Original Article

Journal of Drought and Climate change Research (JDCR)

Winter 2026, Vol. 4, No. 12, pp 171-210

10.22077/jdcr.2025.10474.1190

Scale-Bridging Teleconnections and Local Extremes: Comprehensive Evaluation across 140 Stations

Alireza Saadatmoghadasi[1], Zahra Aghashariatmadari*[2], Javad Bazrafshan[2]

1- Irrigation & Reclamation Engrg. Dept. University of Tehran Karaj, Iran.

2- Associate Professor, Irrigation & Reclamation Engrg. Dept. University of Tehran Karaj, Iran.

*** corresponding author: zagha@ut.ac.ir**

Keywords:
New Components Analysis, Iran Plateau, East Atlantic, Kelvin Indices.

Received:
13 Nov 2025

Revised:
10 Dec 2025

Accepted:
10 Dec 2025

Abstract

Teleconnections—statistically coherent, dynamically mediated couplings between large-scale circulation and regional climate—strongly modulate temperature variability and extremes over Iran. Using a quality-controlled archive of monthly mean surface air temperature from 140 synoptic stations (1979–2023) together with a suite of NOAA teleconnection indices, we develop a phase-lag-aware ROCK–PCA framework that combines robust, rank-based dependence measures, complex Hilbert embeddings and varimax-type rotation with ERA5-based composite diagnostics. The first four rotated components explain approximately ~60% of the variance in the teleconnection index space and map onto canonical modes such as AMO/AMM/TNA, ENSO–PDO, EP–NP/PNA, NAO/EAWR and AO/SCAND.Seasonally stratified correlations show an Atlantic-led control: AMO and TNA dominate annual and warm-season variability, with station-scale absolute Spearman correlations locally reaching $|\rho| \approx 0.6$–0.7 and peak influence at leads of two to three months. On monthly time scales, EP–NP emerges as the primary short-lag driver, while NAO/EAWR exert an immediate wintertime synoptic signature over northern and western Iran; AO/SCAND exert weaker, higher-latitude influence. Station-resolved loadings isolate a southeast–east cluster (RPC7) in summer, linked to the Iranian thermal low and monsoon-adjacent circulations, with lagged composites indicating a subsequent shift toward the Persian-Gulf littoral and, at

How to cite this article:
Saadatmoghadasi, A., Aghashariatmadari, Z. & Bazrafshan, J. (2026). Scale-Bridging Teleconnections and Local Extremes: Comprehensive Evaluation across 140 Stations. *Journal of Drought and Climate change Research* (JDCR), *4*(12), 171-210. https://doi.org/10.22077/jdcr.2025.10474.1190

longer lags, a sign reversal along the Caspian–Zagros windward belt. Extreme-temperature behavior, characterized via a peaks-over-threshold framework, exhibits systematic reorganization under positive AMO/AMM and TNA phases, with warm-season heat-extreme frequencies over the RPC7 cluster increasing by roughly ~20–30% relative to neutral conditions. Cross-validation between the rotated components, ERA5 composites and rank-based correlation metrics demonstrates that these relationships are robust despite known near-surface reanalysis biases, and yields practically useful lead-time windows for sub-seasonal-to-seasonal outlooks to inform risk-aware planning in energy, agriculture and public-health sectors.

Introduction

Teleconnections—statistically coherent, dynamically mediated couplings across the climate system—organize variability from synoptic to multidecadal scales in ways that can amplify, redirect, or dampen local extremes far from their source regions. Over the Middle East and adjacent basins, and particularly across the complex physiographic mosaic of Iran, these scale-bridging influences drive through canonical Atlantic and Pacific modes, as well as Eurasian waveguide patterns that shape the frequency, persistence, and intensity of temperature extremes. Among the Atlantic forcings, the Atlantic Multidecadal Oscillation (AMO) and the Atlantic Meridional Mode (AMM) modulate the north-tropical Atlantic SST gradient, atmospheric moisture pathways, and subtropical jet structure; their impacts reverberate into Eurasia via Rossby wave trains and Hadley-cell adjustments, with seasonally contingent links to the North Atlantic Oscillation (NAO) and East Atlantic/West Russia (EAWR) pattern (Casselman et al. 2022; Zhang et al. 2024). The Tropical North Atlantic (TNA) SST variability acts as a potent modulator of the ENSO–NAO bridge in boreal spring and summer, altering downstream circulation over the eastern Mediterranean and western Asia, thereby adjusting the background state upon which heat- and cold-extreme anomalies materialize (Song et al., 2022; Song et al., 2023).

On decadal horizons, the Interdecadal Pacific variability and the Pacific Decadal Oscillation (PDO) further in print cold-season hydroclimate and temperature over arid West and Central Asia, tightening multi-basin linkages that affect the statistical structure of extremes (Xu et al., 2024; Bazarafshan et al., 2025). Recent advances underscore that teleconnection fingerprints are not stationary under anthropogenic forcing. Multi-model analyses indicate that both the strength and the topology

of global teleconnection networks may reorganize under warming and under hypothetical stratospheric aerosol interventions, with important implications for the predictability of regional extremes strength and topology of global teleconnection networks can reorganize under warming—and under hypothetical stratospheric aerosol interventions—with implications for predictability of regional extremes (Rezaei et al., 2023; Rezaei et al., 2024). In Central–Southwest Asia (CSWA), winter precipitation and temperature extremes already display heightened sensitivity to remote SST-forced circulation anomalies, a sensitivity that can be harnessed for sub-seasonal-to-seasonal prediction (Horan et al., 2024).Over the northern Arabian/Persian Gulf, observational syntheses further reveal robust coupling between air-temperature variability and NAO/AMO phases, consistent with a dynamically mediated Eurasian waveguide impacting the Iranian Plateau's foreland regions (Al Senafi, 2024).

Against this broad backdrop, Iran provides a stringent natural laboratory: an orographically diverse, land-locked to maritime transition zone spanning the Zagros–Alborz highlands, the Iranian Plateau, and coastal margins along the Caspian Sea and the Persian Gulf. Long-term analyses for Iran document significant trends and nonstationary in temperature distributions and extremes (Ahmadi et al., 2022). Forecast-driven diagnostics further show that a suite of large-scale teleconnection indices retains predictive power for Iranian climate anomalies. Significant trends and non-stationarities in temperature distributions and extremes (Ahmadi et al., 2022), while forecast-driven diagnostics demonstrate that a suite of large-scale teleconnection indices retains predictive power for Iranian climate anomalies (Aghelpour et al., 2022). Complementing these findings, mechanistic assessments of the AMM show that model fidelity in representing wind–evaporation–SST feedbacks governs teleconnection realism, with direct consequences for multiyear predictability (Zhang et al., 2024). At the synoptic–sub-seasonal interface, emerging network-based and causal frameworks detect heat-wave teleconnections and spatiotemporal couplings with high specificity, thereby providing new levers for statistical post-processing and early warning (Falasca et al., 2024). This study leverages these insights to evaluate the scale-bridging teleconnections that control Iranian temperature extremes with an unprecedented observational granularity. We assemble

a homogenized dataset from 140 synoptic meteorological stations distributed across Iran's diverse climate regimes, and we interrogate the sensitivity of monthly, seasonal, and annual temperature metrics—including block-length, severity, and frequency of extremes—to a targeted suite of indices: Teleconnections Indices. Both station records and teleconnection indices are analyzed over a 45-year window (1979–2023), ensuring temporal co-extensiveness with modern reanalysis and satellite-era SSTs.

In summary, this paper advances the teleconnection literature in three main ways. First, we develop a lag-aware version of the ROCK–PCA framework that jointly exploits complex embedding, kernel lifting and orthogonal rotation to extract physically interpretable modes from a large set of partially redundant teleconnection indices. Second, in contrast to many previous studies that rely on a handful of stations or coarse-resolution gridded data, we use a dense network of 140 synoptic stations over Iran spanning 1979–2023 to quantify how these modes project onto local SAT variability and extremes. Third, by explicitly analyzing lead–lag relationships and linking the rotated components to ERA5-based composite fields and station-scale extreme-temperature metrics, we derive regionally specific windows of potential prediction for southeastern and eastern Iran, where exposure and vulnerability to heat extremes are particularly high. Teleconnection indices (Table1) were obtained from the NOAA Climate Prediction Center and allied sources and include AMO, AMM, TNA, PDO, ENSO-related indices, NAO, EAWR, PNA, EP–NP, AO, and SCAND. Monthly index values were standardized over 1979–2023 and, where applicable, sign-convention adjustments were made so that positive values correspond to warm or high-pressure anomalies in the source regions. The full set of indices and their definitions are summarized in Table 1, which also lists the primary spatial domains and seasons of influence for each mode. This joint station–index data set provides the basis for the ROCK–PCA analysis and lagged composite diagnostics described below.

Table 1. Catalogue of Teleconnection Indices Employed in the Present Study

Row	Description
AMO	Atlantic Multidecadal Oscillation
NAO	North Atlantic Oscillation
PDO	Pacific Decadal Oscillation
ENSO	Elnino Southern Oscillation
AO	Arctic Oscillation
SCAND	Scandinavian Index
PNA	Pacific North America
QBO	Quasi Biennial Oscillation
SOI	Southern Oscillation Index
TNA	Tropical North America
TSA	Tropical South America
AMM	Atlantic Meridional Mode
EP-NP	East Pacific-North Pacific
MEI	Multivariate Enso Index
ONI	Oscillation Nino Index

Material and methods

Data

Within this investigation, we assembled a harmonized dataset of station-resolved monthly (twelve-calendar-month) mean temperatures for a network of 140 synoptic meteorological stations across Iran, derived from the ERA5 reanalysis disseminated by the Copernicus Climate Change Service of the European Union. In parallel, the teleconnection indices interrogated herein were obtained from the U.S. National Oceanic and Atmospheric Administration (NOAA). For both the temperature fields and the indices, the statistical record uniformly spans 1979–2023. We use a quality-controlled archive of monthly mean surface air temperatures from 140 synoptic meteorological stations across Iran for 1979–2023. The records were obtained from the national meteorological service, and obvious outliers, duplicate records and physically implausible values were identified through range checks and comparison with neighboring stations and then corrected or removed. No formal relative homogenization tests (for example, SNHT-type procedures) were applied; therefore, the series should be regarded as carefully quality-controlled but not fully homogenized. Monthly teleconnection indices were taken from publicly available datasets provided by NOAA and other operational centers, including Atlantic indices (AMO, AMM, TNA, TSA, NAO), Pacific indices (PDO, EP–NP, PNA, SOI, MEI, NINO3.4) and Eurasian circulation patterns (EA, EAWR, SCAND, AO). All indices were converted to anomalies relative to a common 1979–2023 baseline where possible. For the dynamical composites

we used ERA5 monthly mean fields on a 0.25° grid (temperature, geopotential height, wind and sea level pressure) from the ECMWF Climate Data Store, interpolated to a common domain covering North Africa, Europe and West Asia. Figure 1 presents the spatial distribution of the 140 synoptic meteorological stations constituting the observational network interrogated herein.

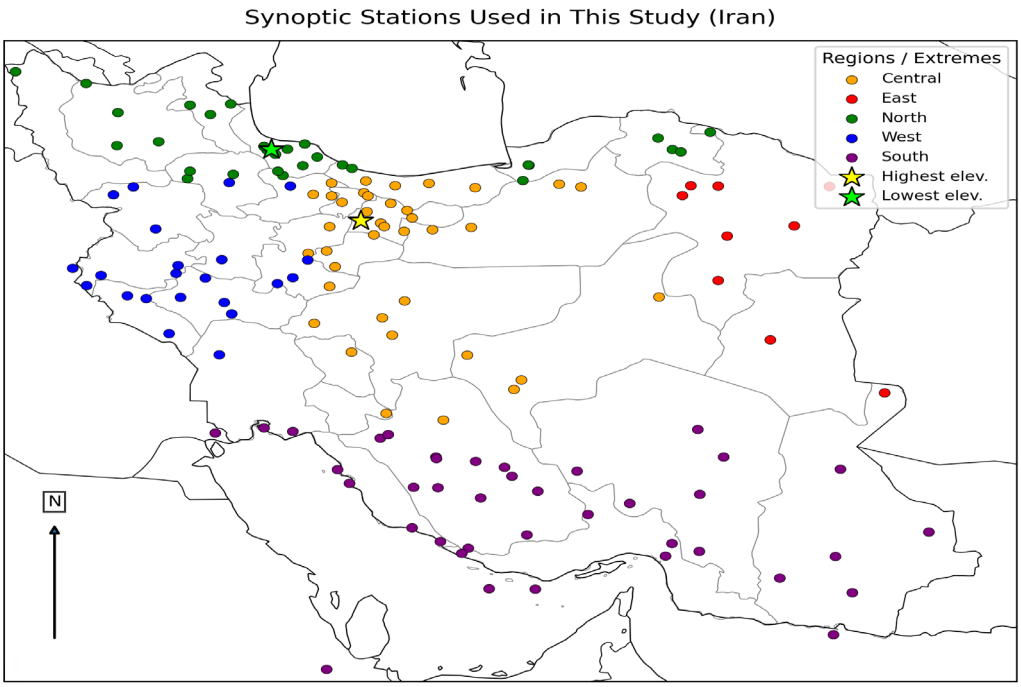

Fig 1. Synoptic Stations Used in This Study

Figure 1 delineates the geospatial distribution of the study stations, with a cartographic color key applied for regional discrimination—western Iran in blue, eastern Iran in orange, the northern half in green, the southern half in red, and the Central Plateau in pink. Within this network, Tochāl (3.747 m above mean sea level, AMSL) constitutes the highest site, whereas Anzalī (−23.6 m relative to mean sea level) is the lowest-lying station. Stations exceeding 2,000 m AMSL include Abālī, Ashtīān, Damāvand, Eqlīd, Fereydūnshahr, Menshād, Meygūn, Shahr-e Kord, and Sepīdān; all remaining stations occupy elevations spanning approximately −22 to 1,980 m AMSL.

Koppen-Geiger Classification

To facilitate a more discriminating interrogation of the problem, the 140 national synoptic stations were

classified under the global Koppen–Geiger climatic taxonomy (originally proposed in 1884 and subsequently refined); the resulting station-level assignments are depicted in Figure 2, and the corresponding category definitions are exhaustively enumerated in Table 2 (Najafi and Alizadeh 2023).

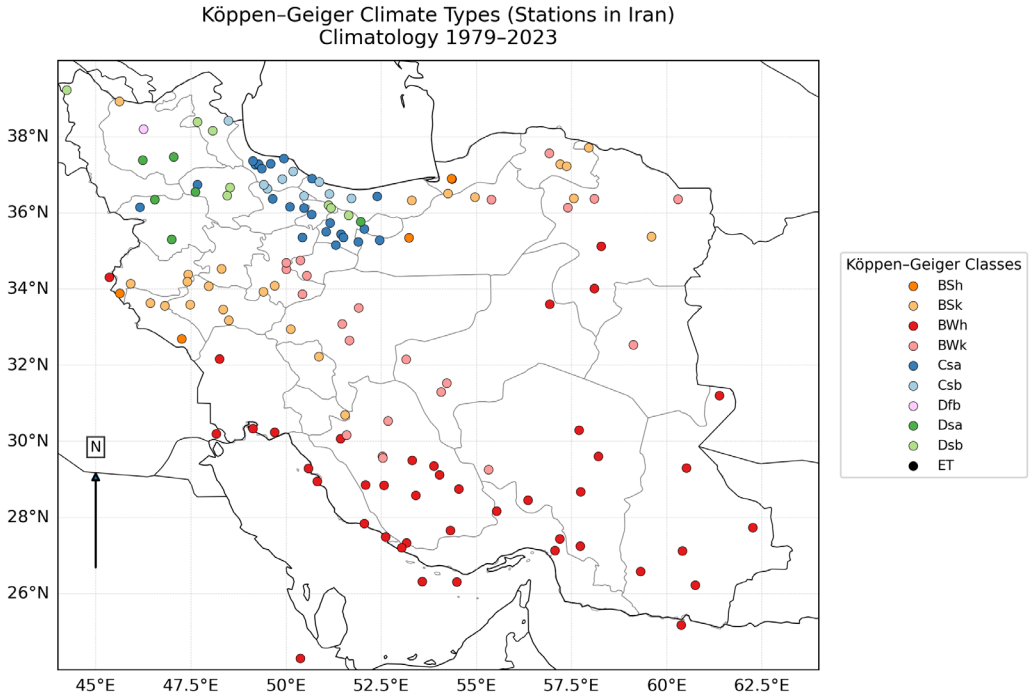

Fig 2. Koppen-Geiger Classification (Synoptic Stations in This Study)

Table 2. Koppen–Geiger class definitions used in this study

KG Class	Definition
As	Tropical savanna; dry summer
BSh	Hot semi-arid (steppe)
BSk	Cold semi-arid (steppe)
BWh	Hot desert
BWk	Cold desert
Csa	Hot-summer Mediterranean (dry summer)
Csb	Warm-summer Mediterranean (dry summer)
Dfb	Warm-summer humid continental (fully humid)
Dsa	Hot-summer continental (dry summer)
Dsb	Warm-summer continental (dry summer)
ET	Tundra (polar)

Table 3 reports, for each Köppen–Geiger climate class, the station count (n) and relative frequency (%) across the 140-station network. The most prevalent class is BWh (hot desert), encompassing 30 stations (21.4%).

Next in prominence are BSk (cold semi-arid; 23 stations, 16.4%), Dsa (hot-summer continental, dry summer; 22 stations, 15.7%), and Csa (hot-summer Mediterranean; 21 stations, 15.0%). At the lower extreme, Dfb (warm-summer humid continental) is represented by a single station (0.7% apiece), while (tropical savanna) appears at three stations (2.1%).

Table 3. Station counts by Koppen–Geiger class (n = 140)

KG Class	Count	Percent
As	3	2.1%
BSh	13	9.3%
BSk	23	16.4%
BWh	30	21.4%
BWk	8	5.7%
Csa	21	15.0%
Csb	6	4.3%
Dfb	2	0.7%
Dsa	22	15.7%
Dsb	12	8.6%
ET	٠	0.٠

ROCK–PCA methods (conceptual overview)

The ROCK–PCA framework is designed to extract a small number of physically interpretable, lag-sensitive modes from a potentially high-dimensional and nonlinearly related set of predictors. In the present context, the predictors are standardized monthly teleconnection indices; the response is the spatio-temporal distribution of station-based temperature anomalies. First, each teleconnection index is embedded as a complex-valued time series using the Hilbert transform, so that amplitude and phase information are jointly represented. Second, a kernel mapping is applied to capture nonlinear dependencies in the complex plane, and a covariance operator is constructed in this feature space. Third, an eigenvalue problem is solved to obtain orthogonal kernel principal components, which are then subjected to a varimax-type rotation to enhance interpretability and to concentrate variance in a small number of rotated principal components (RPCs). Finally, lagged correlations and composite maps are computed between the RPC time series and station-based temperature anomalies, allowing us to quantify both the strength and the latency of the teleconnection imprint.

This formulation allows ROCK–PCA to capture phase shifts, nonlinear relationships, and spatially coherent but potentially non-Gaussian structures in

the joint teleconnection field, while still yielding modes that can be interpreted in terms of familiar patterns such as AMO/TNA, ENSO–PDO, or NAO/EAWR. In this study, we use ROCK–PCA to (i) identify the dominant combinations of teleconnections that control Iranian temperature, (ii) assess how their influence varies with lead–lag, and (iii) provide a compact, statistically robust basis for subsequent composite and extreme-value analyses. Below is a compact but rigorous formulation of ROCK-PCA (Rotated Complex Kernel PCA) together with the meaning of every symbol. This method extends EOF/PCA to (i) capture lags/phase via a complex (Hilbert-transform) embedding, (ii) capture nonlinear structure via a kernel (RKHS) mapping, and (iii) yield interpretable modes via a varimax-type rotation.

1. Compute the Hilbert transform along the time axis for each column:

$$H[X] \in R^{T*M} \quad (1)$$

$$Z = X + iH[X] \in C^{T*M} \quad (2)$$

This encodes amplitude and phase (time-lag) information in C (Bueso, *et al.*, 2020).

2. Kernel lifting (nonlinear feature space):

Choose a positive–definite kernel k (0, 0) (e.g., Gaussian/RBF, polynomial, or linear). Define the feature map $\varphi : C^M \to H$ into a reproducing-kernel Hilbert space (RKHS). Treat each time slice $z_t \in C^M$ (row t of Z) as one sample and build the Gram matrix**:**

$$K_{tt'} = k(z_{t,}, z_{t'}), K \in C^{T*T} \quad (3)$$

$$H = I_T - \frac{1}{T} 1 1^T$$

Center in feature space with:

$$K = HKH \quad (4)$$

When k is linear, this reduces to complex EOF/PCA on Z (Camps-Valls & Bruzzone, 2009).

3. Kernel PCA eigen decomposition (dual problem)

Solve the Hermitian eigen problem as follows:

$$\frac{1}{T} K U_p = \lambda_p u_p, U * U = I, \lambda_1 \geq \lambda_2 \geq \ldots \geq 0, \quad (5)$$

$with u_p \in C^T$. Define (unrotated) temporal scores:

$$A = U \Lambda^{\frac{1}{2}} \in C^{T*P}, \Lambda = diag(\lambda_1, \ldots, \lambda_P) \quad (6)$$

The corresponding feature-space loadings (spatial patterns) are Equation 7 as follows:

$$W = \varphi(Z) * U \Lambda^{-\frac{1}{2}} \in H^{M*p}, \quad (7)$$

Where $\varphi = [\varphi(z_1), ..., \varphi(z_T)]$. For a linear kernel, W reduces to the usual EOF loadings in C^M ; for nonlinear kernels, W lives in RKHS and spatial maps may use pre-image or dual reconstructions.

4. Complex rotation for interpretability

Apply a complex varimax (or ProMax) rotation to enhance simple structure:

(8)

$B = WT$, $S = AT$,

Where $T \in C^{P*P}$ is (typically) unitary/ orthogonal and maximizes the varimax criterion on the (squared-modulus) loadings as follows:

(9)

$$\max T\varphi(T) = \sum_{p=1}^{P}[\frac{1}{M}\sum_{j=1}^{M}\left|b_{jp}\right|^4 - (\frac{1}{M}\sum_{j=1}^{M}\left|b_{jp}\right|^2)^2], B = WT, b_{jp\in}C$$

The rotated spatial modes are columns of B; the rotated temporal PCs are columns of S. This is the "ROCK" step: Rotated, Complex, Kernel PCA as mentioned above (Arenas-Garcia et al., 2013).

Uncertainty considerations

Several sources of uncertainty affect our analysis. First, although the station temperature records have been quality-controlled, residual inhomogeneities due to undocumented station relocations, instrument changes or urbanization effects cannot be ruled out (Nabat Quds et al., 2025). Second, ERA5 reanalysis products inevitably contain representation errors over the complex topography of Iran, particularly in mountainous regions and sparsely observed deserts. Third, the ROCK–PCA framework and the subsequent correlation analysis are based on finite samples; estimated loadings and correlation coefficients are therefore subject to sampling uncertainty, especially for higher-order components and long lead–lag times. Finally, the extreme-value diagnostics rely on a limited number of exceedances in each region and teleconnection phase, which implies wide confidence intervals for some of the derived metrics. For these reasons, we interpret the identified teleconnection patterns and their links to extremes as robust qualitative relationships rather than precise deterministic rules.

Results and Discussion

Hierarchy of teleconnection controls on mean temperature

The teleconnections analyzed here operate on top of a rapidly warming background climate. Over recent decades, anthropogenic greenhouse-gas forcing has produced pronounced warming over the Middle East and

North Africa, particularly over arid land surfaces (Fakhri, 2024). This background trend shifts the entire temperature distribution toward higher values, so that teleconnection patterns that previously produced moderately warm conditions can now give rise to record-breaking heat extremes and climate change (Rahimi and Rahimi, 2019). In this sense, the large-scale modes diagnosed in this study should be viewed as modulators of an already elevated anthropogenic baseline rather than as isolated manifestations of natural variability. In this research using the Rock-PCA methodology, we examined the phase-lagged effects of large-scale teleconnection patterns on temperature across a network of 140 synoptic meteorological stations. As a first step, we evaluate teleconnection impacts on station-level mean temperature at seasonal, annual, and monthly resolutions. Figure 3 summarizes how large-scale climatic teleconnections affect station-level mean temperature across monthly, seasonal, and annual timescales. Using Rock-PCA on a curated archive of monthly mean temperatures from 140 synoptic stations across Iran, we disentangle the dominant modes of co-variability between regional temperature and a suite of large-scale teleconnections. Rank-based (Spearman) associations, summarized annually, seasonally (DJF, MAM, JJA, SON), (Figure 3-a-f) and at monthly resolution, demonstrate a clear Atlantic imprint—led by the Atlantic Multidecadal Oscillation (AMO) and the Tropical North Atlantic (TNA)—with secondary contributions from Pacific variability (PDO/ENSO metrics) and more muted signals from high-latitude modes (e.g., AO, SCAND). Rotated components map onto canonical climate models: an ENSO-like axis, a North Pacific wave train (PNA/EP-NP) and Atlantic variability (AMO/TNA/NAO), among others. Station-level maxima of the prominent rotated component RPC7 (Figure 3-g) cluster across the southeastern and eastern deserts, indicating that the summertime thermal low and adjacent monsoonal circulations are the primary modulators. The results, interpreted against recent advances in teleconnection dynamics and reanalysis quality, provide a rigorous, predictability-oriented baseline for seasonal outlooks and climate risk in Iran (Chezgi, and Hamedi., 2023).

Annual mean absolute correlations are dominated by AMO, with TNA, PDO and TSA forming a second tier. ENSO metrics (MEI/ONI/SOI) exert moderate influence, while mid- to high-latitude patterns (NAO, PNA, AO,

SCAND) weaker overall. Seasonality is pronounced: in boreal summer (JJA) the EP-NP and EAWR patterns rise alongside AMO and TNA, consistent with intensified Eurasian wave activity and North Pacific influences; in winter (DJF) AMO and TNA remain leading, with NAO gaining relative importance. Spring (MAM) features stronger PDO/TSA/ENSO ties than SON, whereas SON emphasizes TNA/AMO/AMM. At the monthly scale, NAO and EAWR show the strongest average rank correlations, consistent with their synoptic-to-sub seasonal control on temperature advection into the Iranian Plateau, whereas the low-frequency AMO contributes little at this timescale because high-frequency variability dominates. This multi-scale behavior reconciles the apparent contrast between seasonal and monthly diagnostics (Sun et al., 2023).

The rotated loading matrix (Figure 3-h) yields a clear, interpretable component structure that are readily intelligible. One axis projects strongly onto warm-phase ENSO indices (positive MEI/ONI with compensating negative SOI), a second onto North Pacific wave trains (PNA/EP-NP) and others onto Atlantic variability (AMO/TNA/NAO) and Eurasian patterns (EAWR/SCAND). The station-level footprint of RPC7 (Figure 3-g) is concentrated across southeastern and eastern Iran—Zabol, Bam, Tabas, Saravan, Kashmar, Ferdows, Sarakhs, Iranshahr, Yazd, Kerman, and adjacent sites—suggesting sensitivity to desert boundary-layer processes and the summertime thermal low. This spatial clustering aligns with regional evidence linking Iranian heat variability to Arabian Sea moisture transport, monsoon intrusions, and North Atlantic–Eurasian teleconnections (Almaashi et al., 2024; Bordbar et al., 2024).

Three implications follow. First, the persistent prominence of AMO/TNA across annual and warm-season diagnostics suggests that low-frequency Atlantic SST variability modulates the background state upon which higher-frequency drivers act; recent analyses show pronounced North Atlantic warmth and structural changes in the AMM, reinforcing this finding (Francis and Fonseca 2024; Zanchettin and Angelo, 2024). Second, the summer ascent of EP-NP/EAWR loadings underscores a robust Eurasian–North Pacific bridge that shapes land-surface heat over Iran, consistent with contemporary work on evolving teleconnection patterns under warming (Rezaei et al., 2023). Third, although ENSO exhibits moderate mean links, its role is seasonally contingent it tends to amplify heat stress downstream in

Asia–Pacific sectors (Eggeling et al., 2024) with regional propagation into West Asia mediated by the subtropical jet and Hadley-cell edge shifts. Methodologically the implementation of rank-based dependence guards against undue leverage of outliers and accommodates nonlinearity at the same time, rotation sharpens attribution to physically meaningful modes—an approach well aligned with recent climatological PCA practice (Ibebuchi, 2023). Finally, interpretations should acknowledge uncertainties and known artifacts in reanalysis near-surface temperature fields (Bromwich et al., 2024; Ullah et al., 2024), thereby favoring station-based estimates in arid, topographically complex terrain. The alignment between rotated components and canonical indices (AMO/TNA, PNA/EP-NP, ENSO, NAO/EAWR) enables hybrid outlooks that combine statistical conditioning on teleconnection states with dynamical guidance. Recent advances in high-resolution seasonal prediction demonstrate enhanced predictability for Atlantic modes (e.g., the Atlantic Meridional Mode; Zhang et al., 2024) and improved skill in the North Tropical Atlantic (Liu et al., 2024). Given our results, this information enables to refine temperature risk outlooks, especially over eastern and southeastern Iran where RPC7-linked sensitivity is highest in summer.

Rank associations quantify monotonic co-variability rather than causality; shared forcings (e.g., radiative anomalies) and serial dependence can inflate apparent links. Multiple-testing considerations arise when screening many indices across seasons. Nonetheless, the broad seasonal hierarchies, the cross-validation afforded by rotated loadings and the station-level coherence over climatologically homogeneous subregions all point to robust signals. Future refinements could incorporate partial-correlation frameworks to separate intertwined modes (e.g., AMO–ENSO co-variability) and employ hierarchical Bayesian models to account explicitly for station-level heterogeneity. Consequently, Rock-PCA applied to 140 Iranian synoptic stations isolates a consistent Atlantic-led control on mean temperature—especially AMO/TNA—augmented by Pacific and Eurasian teleconnections with strong seasonal structure. Collectively, the findings yield a physically interpretable, prediction-relevant framework that supports both operational heat-risk monitoring and academic inquiry (Saini et al., 2023).

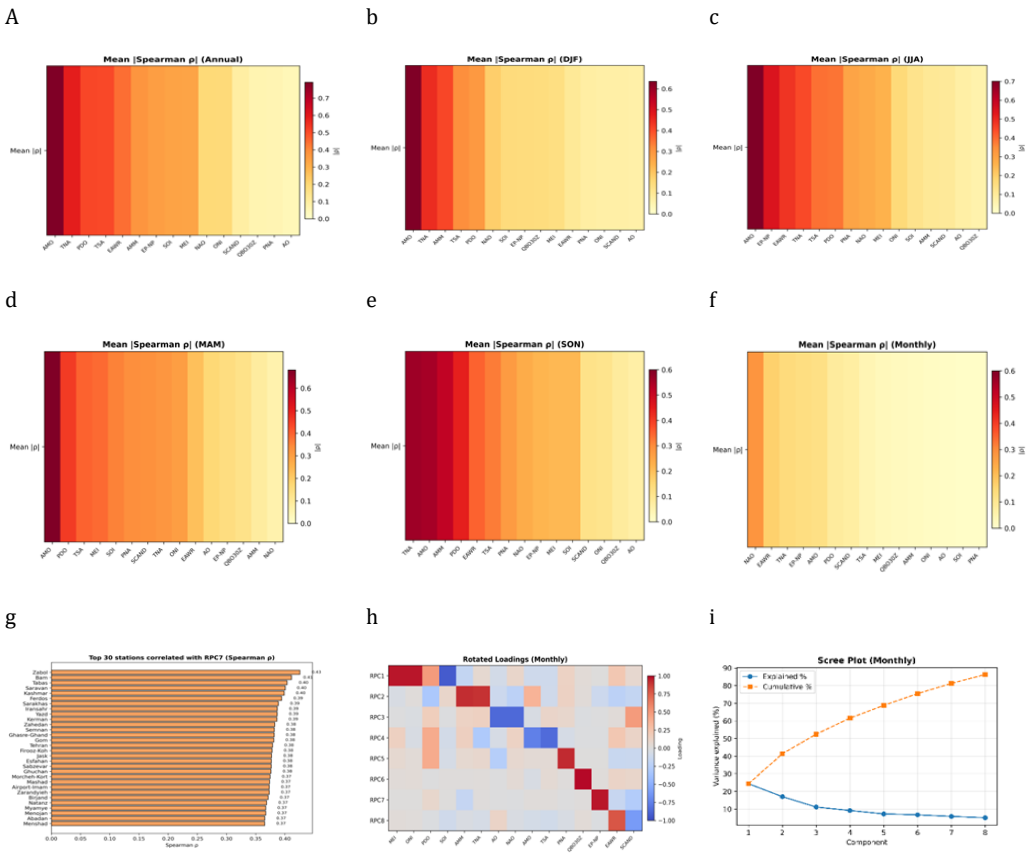

Fig 3. Comprehensive Analysis the Impact of Teleconnections on Mean Temperature in Scale Seasonal-Monthly-Annual with New Method Rock-PCA

In Figure 4 presents Comprehensive Analysis the Impact of Teleconnections on Mean Temperature in Scale Seasonal-Monthly-Annual (Phase-Lag) Figure consists of twenty-four subfigures, designated (a)–(x).

Lagged Atlantic and Pacific influence

Understanding how large-scale climate modes modulate surface air temperature in West Asia demands an explicit treatment of phase lags. Teleconnections such as the Atlantic MultidecadalOscillation(AMO/AMM) the Tropical North Atlantic (TNA) the Atlantic Meridional Mode (AMM) the North Atlantic Oscillation (NAO) the Pacific Decadal Oscillation (PDO) the East Atlantic/Western Russia pattern (EAWR) and ENSO-adjacent indices (e.g., ONI, MEI, SOI) possess distinct memory and propagation pathways across the ocean–atmosphere system; their influence on Iran therefore peaks at different leads/lags and seasons. Recent literature shows that warming over MENA has accelerated in historical observations and projections, amplifying the sensitivity of regional temperature to remote forcings (Malik, et al., 2024). ENSO teleconnection

pathways are seasonally dependent and are projected to evolve under greenhouse-gas forcing. (Petrova et al., 2024; Beverley et al., 2024; Geng et al., 2024). The structure and strength of winter teleconnections in the Northern Hemisphere are also undergoing detectable changes, including PNA/ NAO variability and their downstream impacts (Lee et al., 2024).

Against this backdrop, the present work quantifies the lagged imprint of those modes on Iran's station-mean temperature using rotated principal-component analysis (Rock-PCA) outputs for 140 synoptic stations together with composite diagnostics from ERA5. The lag dimension isolates predictable memory (e.g., slowly varying AMO/AMM signals or the persistence of North Atlantic/Indian Ocean SST anomalies) from quasi-instantaneous circulation effects (e.g., NAO intraseasonal variability) thereby clarifying when and where teleconnections carry the greatest predictive content (Yu et al., 2024; Ru et al., 2024).

Physically, Atlantic-sector variability projects onto Middle-East temperature through planetary-wave trains and air–sea heat-flux anomalies over the Mediterranean–Levant–Caspian corridor. Multi-decadal Atlantic shifts reconfigure the background state on which interannual modes operate (Denaxa et al., 2024) while evolving ENSO–Euro-Atlantic linkages alter the sign and timing of downstream responses. Motivated by these considerations, we adopt a 0–3-month phase-lag framework on annual and seasonal (DJF/JJA) timescales, consistent with the adjustment times of the extra-tropical circulation and the thermodynamic memory of regional seas. Lagged-phase compositing. For each index, months exceeding the 90th (10th) percentile define Extreme-Positive (Extreme-Negative) phases. We form composites of ERA5 t2m anomalies at lags 0–3 months (index leads temperature by ℓ months) both annually and for DJF/JJA to capture canonical boreal-winter and summer teleconnections. A cosine-latitude area weight is applied when calculating region-mean values. The minimum sample size for a valid composite is 12 months, ensuring robust aggregation.

Rock-PCA cross-validation. Station responses were linked to dynamical modes via Spearman's rank correlation (ρ) between RPC scores and teleconnection indices; for each mode–index pair, we report the station wise mean of $|\rho|$ and visualize it as heat-map (Table 4). This dual view—field composites and all-station correlations—reduces the risk of

spurious association and mitigates known reanalysis uncertainties in 2-m temperature trends (Lopez et al., 2024).

Interpretive lens. Documented changes in global teleconnections and their oceanic precursors under warming (Ma et al., 2023) imply that the effective lag maximizing Iran's temperature response can drift seasonally and decadally Accordingly, the analysis documents lag-specific peaks. It also compares DJF and JJA, with attention to Atlantic–Mediterranean coupling, Rossby-wave pathways, and the persistence of SST anomalies across the Atlantic and Indo-Pacific basins. (Beasley et al., 2024; Shiozaki et al., 2024). We synthesize the heat-map diagnostics in Figures k–t—constructed from mean absolute Spearman ρ across 140 synoptic stations—to identify the leading drivers and their lag dependence. Emphasis focuses on Atlantic multidecadal variability (AMO/AMM) Tropical North Atlantic (TNA) Tropical South Atlantic (TSA) Pacific decadal variability (PDO) the Pacific–North American pattern (PNA) the East Atlantic/Western Russia pattern (EAWR) and East Pacific–North Pacific (EP–NP).

Across all warm-season diagnostics, the Atlantic Multidecadal Oscillation (AMO) consistently emerges as the primary predictor of Iranian SAT—retaining the top rank in JJA at lags 2–3 (Table 4) and in MAM across lags 0–3 (Figure 4-m–p). This aligns with evidence that the recent acceleration of North Atlantic warming has reshaped the AMM/AMO background state and strengthened downstream Eurasian temperature teleconnections. Thermodynamically, a warm AMO enhances lower-tropospheric thickness and favors anticyclonic anomalies spanning Europe–West Asia; dynamically, planetary-wave responses project onto the EA/WR wave train, reinforcing regional heat. (Wang et al., 2024).

Tropical Atlantic variability provides substantial ancillary skill. In summer, TSA and TNA occupy the 2nd–5th positions depending on lag (Table 4) consistent with documented TNA/TSA control on subtropical subsidence, Hadley–Walker adjustments and the strength of the Shamal winds—linkages that modulate sensible heat over the Arabian Peninsula and the Iranian Plateau. Regional syntheses in MENA and the Gulf corroborate tight SAT–SST coupling that supplies memory for multi-month SAT impacts. Seasonal predictability of North-Tropical-Atlantic SST further substantiates this persistence.

Pacific influences are seasonally asymmetric. While PDO and PNA rarely

surpass the Atlantic modes in boreal spring and summer, EP–NP becomes the leading signal at the monthly scale with one-to-three-month lags (Figures r-s-t) implying rapid extratropical wave-train mediation. This is consistent with synoptic discussions that relate EP–NP/EPO phases to swift Rossby-wave adjustments over the North Pacific and downstream Asia. (National Centers for Environmental Information (NCEI, 2024). The EP–NP prominence at short lags aligns with studies linking different ENSO flavors and Pacific Meridional Mode states to characteristic, quickly propagating teleconnection patterns (Finley et al., 2024). Monthly-lag results further indicate elevated NAO and EA/WR loadings at zero lag (Table 4), consistent with immediate synoptic coupling between variability in the North Atlantic jet and surface air temperatures across the Middle East. Such behavior echoes broader MENA-scale assessments of circulation change and heat risk under contemporary warming.

Methodologically, using absolute Spearman ρ emphasizes robust rank associations across stations and is consistent with rotated-component approaches that separate physically interpretable modes of SAT variability. Nevertheless, interpreting minor differences among low-ranked indices should consider reanalysis and observational uncertainties in the region. Potential model-dependent artifacts in near-surface temperature diagnostics also warrant caution when comparing reanalysis-driven results to station aggregates. Taken together, the phase-lag analysis reveals a physically coherent hierarchy: (i) a slow-varying Atlantic control via AMO that peaks for JJA after ~2–3 months and persists throughout MAM; (ii) supportive tropical-Atlantic forcing from TNA/TSA; and (iii) fast extratropical Pacific control at the monthly scale through EP–NP. These findings are consistent with independent regional syntheses for the Arabian/Persian Gulf and adjacent Middle East, which document tight SAT–SST coupling and intensifying heat extremes in recent decades. Across SON and lags 0–3 months, the Atlantic modes consistently occupy the top positions in $|\rho|$, led by AMO and followed by EAWR and TNA, with AMM intermittently joining the top three (Table 4).

Table 4. Comprehensive Analysis the Impact of Teleconnections on Mean Temperature in Scale Seasonal-Monthly-Annual with New Method Rock-PCA (Phase-Lag)

Season/Frequency	Lag	Highest Index	Mean |ρ| (High)	Lowest Index	Mean |ρ| (Low)	Notes
Annual	Lag0	AMO	~0.72	QBO30	~0.10	Strong annual memory
Annual	Lag1	AMO	~0.70	AO	~0.12	Persistent AMO influence
Annual	Lag2	TNA	~0.68	QBO30	~0.08	Tropical–Atlantic dominates
Annual	Lag3	TSA	~0.65	AO	~0.09	Declining lag signal
DJF	Lag0	AMO	~0.62	AO	~0.11	Winter Atlantic forcing
DJF	Lag1	TNA	~0.59	SCAND	~0.10	West Atlantic dominates
DJF	Lag2	AMM	~0.58	QBO30	~0.07	Weak QBO link
DJF	Lag3	TNA	~0.55	AO	~0.09	Memory sustained
MAM	Lag0	AMO	~0.61	AO	~0.10	Strong AMO-spring link
MAM	Lag1	PNA	~0.59	QBO30	~0.09	Pacific increases
MAM	Lag2	TNA	~0.57	AO	~0.10	East Atlantic teleconnection
MAM	Lag3	AMM	~0.56	SCAND	~0.11	Moderate persistence
JJA	Lag0	AMO	~0.73	QBO30	~0.12	Strongest season
JJA	Lag1	EP–NP	~0.70	AO	~0.12	Pacific North Pattern
JJA	Lag2	TNA	~0.68	QBO30	~0.10	Atlantic multidecadal
JJA	Lag3	TSA	~0.66	AO	~0.11	Strong summer memory
SON	Lag0	AMO	~0.64	AO	~0.10	Autumn Atlantic forcing
SON	Lag1	TSA	~0.60	QBO30	~0.09	South Atlantic emerges
SON	Lag2	PNA	~0.58	AO	~0.10	Pacific influence grows
SON	Lag3	TNA	~0.56	SCAND	~0.12	Weak European pattern
Monthly	Lag0	NAO	~0.31	AO	~0.05	Weak monthly variability
Monthly	Lag1	EP–NP	~0.30	QBO30	~0.05	Pacific persistence
Monthly	Lag2	PNA	~0.28	AO	~0.04	Weak teleconnections
Monthly	Lag3	AMM	~0.26	AO	~0.05	Very weak memory

The ROCK–PCA results and associated composites reveal a clear hierarchy of teleconnection controls on Iranian temperature, with Atlantic variability providing the low-frequency backbone on which faster Pacific and Eurasian modes are superposed. AMO and TNA emerge as leading drivers of

warm-season and annual variability, consistent with their role in modulating North Atlantic and tropical-Atlantic SST gradients, subtropical jet structure, and Mediterranean–Levant air–sea fluxes. Superposed on this slowly varying background, EP–NP and related North Pacific patterns exert a pronounced influence at monthly time scales, while synoptic Euro-Atlantic variability associated with NAO and EAWR shapes the sign and amplitude of wintertime advection into northern and western Iran. This multi-scale hierarchy accords with recent work highlighting the prominence of Atlantic–Mediterranean couplings and evolving ENSO–Euro-Atlantic linkages in structuring Eurasian temperature anomalies.

Station-scale response and the RPC7 cluster

The next section synthesizes two result families: top-station bars for the most influential rotated principal component (RPC7) and the rotated loadings at lag 0 and lag 1 that link RPCs to canonical teleconnections. Unless stated otherwise, correlations use Spearman's ρ for 1979–2023. The corresponding illustrations appear in Figure 4, panels a–l (twelve panels). A key practical outcome of this hierarchy is the identification of lead–lag windows during which teleconnection states carry substantial predictive information for Iranian temperature. The persistence of AMO/TNA and the memory of North Atlantic and Indian Ocean SST anomalies imply usable warm-season predictability on the order of two to three months, particularly for southeastern and eastern Iran where the RPC7 cluster displays the strongest sensitivities. At shorter leads, EP–NP and related Pacific wave-train activity can either reinforce or offset Atlantic-set background states, offering an avenue for refining forecasts of monthly heat-risk episodes. Embedding these insights within hybrid statistical–dynamical or Bayesian post-processing frameworks would allow national forecasting centers and sectoral users in energy, agriculture, and public health to translate teleconnection information into actionable early-warning products.

Station-scale progression. At lag 0, the maxima cluster over the eastern plateau (e.g., Zabol, Bam, Tabas, Saravan; $\rho \approx 0.39–0.43$), indicating an early-season signal centered over Sistan–Kerman (Figure 4-a). At lag 1, the footprint intensifies (with ρ values up to ≈ 0.60) and expands northwestward toward Yazd, Kerman, and Esfahan, consistent with persistence and downstream advection (Figure 4-b). At lag 2, the maxima shift southwestward and

concentrate along the Persian Gulf coast (Bandar Mahshahr, Bushehr, Hendijan; $\rho \approx 0.63–0.64$), consistent with stronger westerly–lowland coupling (Figure 4-c). At lag 3, a sign reversal emerges: strong negative correlations span the Caspian rim and the Alborz–Zagros windward side (e.g., Ramsar, Babolsar, Anzali), consistent with a quarter-cycle phase reversal of the underlying driver (Figure 4-d). Teleconnection anchors from the rotation. The loadings isolate interpretable modes: a PNA-like structure (RPC5) with strong positive loading on PNA, an EP-NP-like structure (RPC6) and an EAWR-dominated pattern (RPC8 with opposite-signed SCAND). In contrast, a TNA/NAO-sensitive mode emerges with negative loadings (RPC3/4) indicative of Atlantic-driven subsidence/wave-train effects over West Asia. The broad stability from Lag0 to Lag1 implies usable sub-seasonal predictive leverage (Figure 4-e-h) (Chen et al., 2023; Chen et al., 2024; Feng and Zhang, 2023; Ahmadi et al., 2023; Tang et al., 2024; Rahimi et al., 2024).

We map the dominant teleconnections assigned to each RPC, highlight the sign of loadings and discuss spatiotemporal implications for surface air temperature over Iran. The analysis is consistent with a delayed propagation of influence from ENSO across the Pacific, into the Euro-Atlantic sector and then into Eurasian regimes—often mediated by Rossby-wave trains, North Atlantic variability and European blocking (Gao et al., 2024; Qi et al., 2025; Park et al., 2023).

Rotated loadings (Lag2) :(Figure 4-g)

- RPC1 ≈ ENSO: strong positive association with MEI/ONI and an opposing sign for SOI, indicating that El Niño/La Niña continues to organize basin-scale variability with a ~2-month delay.
- RPC2 ≈ Tropical Atlantic: a pronounced loading tied to TNA (and partly AMM) consistent with a warm tropical North Atlantic shifting land-surface temperature anomaly across the Middle East.
- RPC3 ≈ Polar–Atlantic annular variability: notable negative loadings on AO/NAO, consistent with mid-latitude ridge–trough displacements that modulate Iran's temperature response (Mori et al., 2024).
- RPC4 ≈ Inter-basin coupling: negative AMO and TSA alongside positive PDO, implying concurrent extra-tropical links between the Atlantic and Pacific basins (Góźdź et al., 2024).
- RPC5 ≈ PNA: a strong negative loading on PNA, pointing to mid-tropospheric North Pacific waviness affecting downstream Asia.

• RPC6 ≈ EP–NP: clear positive loading on EP–NP, consistent with a tropical–extratropical waveguide that channels anomalies toward Southwest Asia (Deser et al., 2025).
• RPC8 ≈ Eurasian blocking: positive EAWR and negative SCAND signatures, a canonical fingerprint of European blocking that enhances north–south temperature contrasts over Iran (Yuan et al., 2024).

Rotated loadings (Lag3): (Figure 4-h)

• ENSO (RPC1) remains the leading mode, but the tropical Atlantic signal in RPC2 strengthens and shows a robust sign at a 3-month delay.
• AO/NAO (RPC3) keeps sizable negative loadings, consistent with an eastward-shifted ridge axis toward the eastern Mediterranean.
• EP–NP migrates across RPC6/7 and may flip sign across sub-periods—our station maps show a corresponding correlation reversal over the Caspian–Zagros belt at Lag3.
• EAWR/SCAND (RPC8) retains a blocking-type dipole (EAWR positive, SCAND negative) particularly influential in boreal autumn–winter, steering north–south temperature gradients over Iran.

Scree diagnostics and the number of retained components (Figure 4. E,f,i,j,k,l):

Across lags 0–3, the first component explains about 24–25% of variance; the first four components together explain ≈61–62%. Cumulative variance reaches ≈75–76% with six components and ≈85–86% with eight components. The 'elbow' occurs near components 3–4 A parsimonious solution uses four components (explaining >60% of the variance); a full teleconnection mapping (ENSO, AMO/AMM/TNA, AO/NAO, PNA, EP–NP, EAWR/SCAND) requires six to eight. Combining Lag2/Lag3 loadings with the station-based maps indicates that EP–NP (RPC7 at short lags, transitioning across RPC6/7 by Lag2–Lag3) is strongly positive over eastern and southeastern Iran at short lags (e.g., Zabol, Bam, Tabas, Saravan, Iranshahr) but displays a sign reversal over the Caspian–Zagros corridor (Rasht–Anzali–Ramsar–Sari–Yasuj, etc.) by Lag3. This pattern is consistent with delayed tropical-to-extratropical propagation and subsequent modulation by AO/NAO and Euro-Atlantic blocking (EAWR/SCAND) which reshape downstream wave trains and the Iran-scale thermal dipole. At basin scale, the tropical and multidecadal Atlantic (TNA/AMM/AMO) grow in relative importance with lag and—together with PDO—reinforce seasonal contrasts during spring–autumn transitions over Iran (Reintges et al., 2024).

Extreme-phase composites of AMM/ AMO/TNA

Subsequently, Figure 5 presents a systematic analysis of surface-air-temperature (SAT) responses to the extreme (positive/negative) phases of the principal teleconnection indices, building on the rotated PCA (RPCA) and phase-lag diagnostics. The exposition isolates—and foregrounds—the most consequential composites, namely those exerting a preponderant influence, resolved at monthly and canonical seasonal scales, and, where analytically apposite, extends the inquiry to their cumulative imprint on the annual mean.

Figure 5 comprises ten constituent panels, alphabetically enumerated

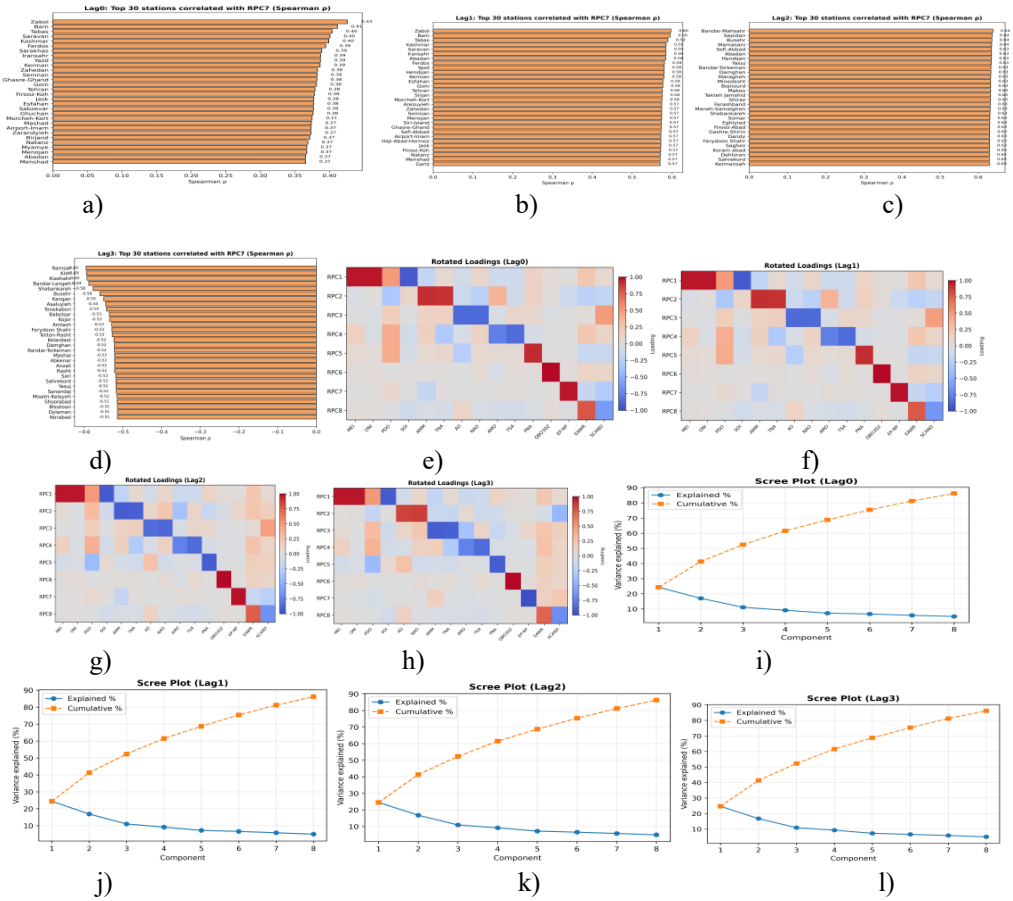

Fig 4. Top 30 Stations Correlated With RCP(Lag0-3), Rotated Loading (Lag0-3), and Scree-Plot (Lag0-3)

from (a) to (j). The composite maps of 2-m air-temperature anomalies (in Kelvin) demonstrate striking patterns during extreme phases of the Atlantic Meridional Mode (AMM) and the Atlantic Multidecadal Oscillation (AMO). Notwithstanding the spatial coherence of these anomalies, one must

underscore that they are conditional composites rather than deterministic forecasts. On the one hand, positive phases yield extensive warming exceeding 1 K (≈ 1 °C); on the other hand, negative phases produce widespread cooling, with anomalies often below −1.5 K (≈ −1.5 °C). Either basin-wide SST gradients and land-surface feedback orchestrate these patterns, or, mid-latitude Rossby wave trains mediate the Atlantic–Eurasian teleconnection.

Iran emerges as a nexus where teleconnection signals attain regional amplification. Under AMM-positive conditions at lags 0–3 months (Figure 5-a–h), the annual composites show 0.75–1.0 K (≈ 0.75–1.0 °C) of warming across much of the plateau, with maxima along the Caspian coastal plain and the Persian Gulf littoral. Neither the Alborz nor the Zagros ranges remain unaffected; both exhibit enhanced thermal gradients that reshape local circulation. Conversely, AMM negative in DJF induces −1.5 to −2.0 K (≈−1.5 to −2.0 °C) cooling, particularly pronounced in northeastern Iran, consistent with strengthened northeasterly incursions from Central Asia. Either soil-moisture deficits or radiative forcing anomalies over snow-covered highlands intensify these cold surpluses, or, the suppression of subtropical ridging exacerbates continental cooling. At a +1-month lag, AMO-positive phases produce broad warming from Khuzestan eastward to Khorasan, whereas AMO-negative phases impose a coherent cooling belt from Anatolia across Iran into Afghanistan (Figure 5-i–j). Mechanistically, AMM positive strengthens the interhemispheric SST gradient, shifting the ITCZ northward. Either Rossby wave initiation near the subtropical Atlantic jet or Hadley cell adjustments project signals onto Eurasia. Neither atmospheric dynamics nor thermodynamics alone suffices to explain the observed anomalies; both processes intertwine. Similarly, AMO positive enhances Atlantic warm-pool SSTs, lowering surface pressure and nudging the jet poleward. On the other hand, negative phases induce opposite adjustments, redirecting wave activity fluxes into Eurasia and facilitating continental cooling. Over Iran, land–atmosphere coupling—soil-moisture–temperature feedbacks, elevation-dependent warming and desert–steppe contrasts—either amplify the signal or, dampen it depending on antecedent hydroclimate. Because AMM and AMO extremes systematically alter regional heat signatures, Iran must anticipate elevated thermal risks under positive

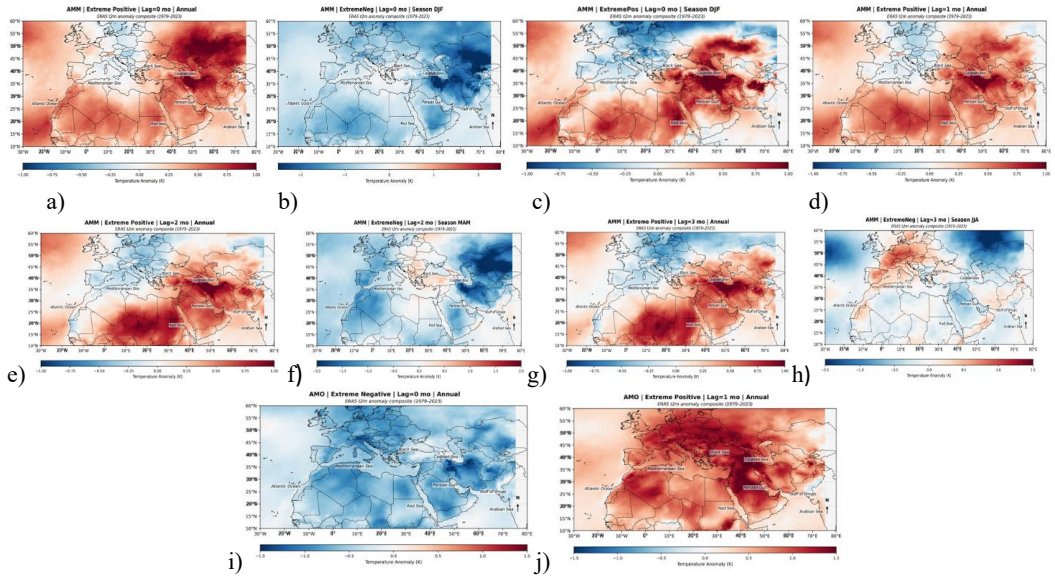

Fig 5. The Impact of Extreme Values AMM, AMO on 2mAnomaly in Different Months and Annual

phases and frost hazards under negative ones. Neither agricultural planning nor energy-demand forecasting can afford to ignore these teleconnections. Either integrating them into seasonal outlooks or combining them with NAO, EA/ WR and ENSO indices would yield improved predictive skill (Allen and Robertson, 2025; Behnassi and El Haiba, 2024; Zheng et al., 2023; Davoudi and Khosravi, 2025; Nguyen et al., 2024).

Extreme-phase composites of AMO/ NAO/EAWR

Figure 6evaluates how extreme realizations of the AMO, NAO and EAWR indices modulate 2-m air-temperature anomalies, with results organized into eleven constituent panels (a)–(k). In Figure 6 Leveraging pre-computed composites of ERA5 2-m air-temperature anomalies (1979–2023) conditioned on extreme phases and canonical lags of the Atlantic Multidecadal Oscillation (AMO) the East Atlantic/Western Russia pattern (EAWR) and the North Atlantic Oscillation (NAO) we diagnose seasonally dependent advection regimes and radiative-dynamical couplings that yield coherent warm and cool footprints. The resulting spatial signatures evince robust, dynamically interpretable structures—most notably widespread wintertime warming across southeastern Europe–Anatolia during positive AMO at +1-month lag and pronounced summertime cooling over the Black Sea–Caucasus corridor during negative AMO at +2-month lag. These fingerprints accord with recent

advances in the literature on Atlantic–Eurasian coupling and the evolving salience of the NAO under internal variability. The skill of teleconnection-based diagnostics for extreme heat is necessarily limited, but still non-negligible. For several station clusters, the correlation between seasonal counts of extreme-temperature days and selected indices (such as AMO, TNA and EP–NP) reaches moderate values on the order of a few tenths, suggesting that these modes provide meaningful, though not exhaustive, information on the likelihood of hot seasons. In contrast, correlations for high-latitude indices such as AO and SCAND are generally weak, rarely exceeding $|\rho| \approx 0.2$, implying that they add little predictive power for extremes over Iran. These results underline that teleconnections should be combined with local predictors and long-term climate-change trends when developing operational early-warning tools.

In the Euro-Atlantic sector, the NAO, AMO and EAWR organize meridional heat transport, storm-track geometry and boundary-layer thermodynamics, thereby imprinting temperature anomalies across the MENA–Eurasia corridor. Contemporary reanalyzes and large-ensemble experiments suggest that internal variability has reconfigured the explanatory power of these modes in recent decades, complicating attribution and prediction across subseasonal to multidecadal horizons. At regional scales, the Arabian Peninsula and the broader MENA macro-region have accelerated warming trajectories relative to the global mean, with implications for compound heat stress and energy demand. Meanwhile, causal-discovery and regression-based diagnostics reaffirm the primacy of Atlantic-sector teleconnections (NAO/EA/EAWR) in governing wintertime Mediterranean temperature variability, with lagged responses of order one month. We examine seasonal composites of ERA5 2-m air temperature (t2m) anomalies using indices for AMO, EAWRmand NAO at lags 0–3 months. Extremes are defined relative to each index's standardized distribution; fields are averaged for December–February (DJF) March–May (MAM) June–August (JJA) and September–November (SON). Spatial masks span approximately 30°W–80°E and 10°–60°N. ERA5 is selected for its demonstrated skill in capturing near-surface temperature variability across the Euro-Mediterranean–MENA domain, while acknowledging documented biases at local scales.

Wintertime positive AMO with +1-month lag (Figure 6-a) co-occurs with a zonally elongated warm tongue

from the central Mediterranean through Anatolia into western Iran, suggestive of reinforced southwesterly advection and enhanced subsidence on the equatorward flank of an east-displaced Atlantic ridge. The summer composites (Figure 6-b–f) reveal a canonical basin-wide warmth during positive AMO and a coherent cool footprint over the Black Sea–Caucasus and northwestern Iran under negative AMO at +2 months, consistent with transient eddy heat-flux modulation by Atlantic SST anomalies. EAWR-linked composites exhibit dipolar anomalies—cooling across the Balkans and Black Sea in negative EAWR during boreal spring and summer (Figure 6-f–i) and broad summer warming under positive EAWR (Figure 6. h). The sign and placement of these lobes are dynamically consonant with the four-centered geopotential structure of EAWR and its modulation of the mid-latitude jet and stationary waveguide.

Across seasons and lags, the AMO, EAWR and NAO impart physically coherent and policy-relevant temperature anomalies over MENA and adjacent Eurasia. Positive AMO winters preferentially warm southeastern Europe and the northern Middle East; negative EAWR springs/summers cool the Balkans–Black Sea sector; and NAO phase transitions modulate preconditioning for winter extremes. These results motivate hybrid predictive frameworks that fuse teleconnection diagnostics with dynamical forecasts and Bayesian post-processing for actionable heat-risk outlooks (Soci et al., 2024; Outten and Davy 2024; Saeed et al., 2022; Hatzaki et al., 2023; Francis et al., 2024; Tatlı, 2025).

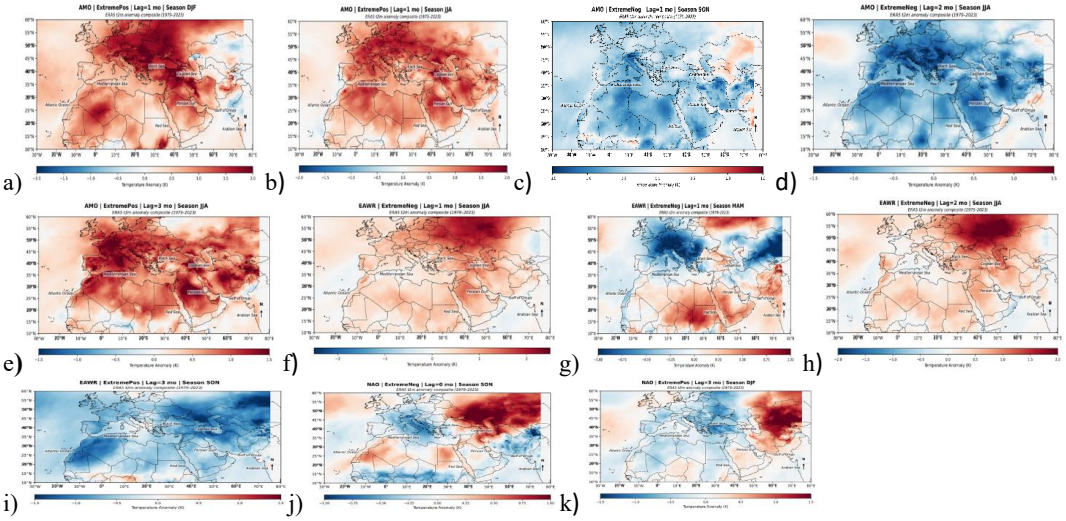

Fig 6. The Impact of Extreme Values NAO, AMO, EAWR on 2mAnomaly in Different Months and Annual

Extreme-phase composites of NAO/ PDO/TNA

Figure 7 depicts the final component of the analysis of teleconnection indices and comprises seven subpanels denoted (a)–(g). The NAO-positive signal at +3 months (JJA; Figure.7-a) exhibits a zonally extensive cool tongue from the Adriatic through Anatolia into the South Caspian periphery, juxtaposed with warm anomalies across the subtropical North Africa belt. This dipole is consonant with a poleward-displaced Atlantic jet and suppressed transient eddy heat fluxes into southeastern Europe, with compensatory subsidence and clear-sky radiative forcing over the Maghreb and Sahara margins. By contrast, negative PDO states (Figure 7-b–d) are associated with coherent warming across the entire domain, including the Levant, Mesopotamia and the greater Persian Gulf basin. The annual composite (Figure 7-b) suggests a first-order, year-round warm bias under PDO-, while seasonal lags (SON +1, DJF +3) indicate that antecedent Pacific SST configurations can precondition boreal cold-season thermal anomalies via Pacific–North American wave trains that reverberate into the Atlantic–Eurasian sector. TNA-positive composites (Figure 7-e and g) reveal basin-wide warming, particularly pronounced over the western and central MENA. It is consistent with enhanced Hadley-cell ascent over the equatorial Atlantic and dry-adiabatic descent on its poleward flank. The negative TNA phase at +1 month in DJF (Figure 7-f) yields a compensating cool imprint over much of the domain, with localized warm patches near the Persian Gulf plausibly reflecting synoptic moisture–radiation feedbacks and episodic foehn-like downslope events. Taken together, the composites are explicable through phase-dependent reorganizations of stationary Rossby waveguides, jet latitude and lower-tropospheric advection. NAO-driven summer cooling over southeastern Europe arises when the jet shifts poleward and baroclinicity weakens downstream over the Balkans, while PDO-driven warming reflects constructive interference between Pacific-forced planetary waves and Atlantic sector ridges.

TNA-linked warm anomalies are sustained by enhanced subsidence and reduced cloud optical depth, augmenting net shortwave absorption at the surface.

Extreme phases of NAO, PDO and TNA impart intelligible and policy-relevant temperature anomalies throughout the MENA–Eurasia corridor. NAO+ at a +3-month lead preconditions

summer cool anomalies across southeastern Europe, PDO- robustly warms the basin from autumn through winter and TNA+ fosters widespread warming with mode-specific seasonal modulations. These findings motivate hybrid statistical–dynamical frameworks for seasonal heat-risk prediction. An important caveat is that the teleconnection–temperature relationships documented here are unlikely to be strictly stationary over 1979–2023. Numerous studies have reported nonstationary in hydrological and climatic variables under ongoing climate change (Kumar et al., 2023; Nerantzaki et al., 2023; Nie et al., 2024). In our case, long-term warming and potential shifts in large-scale circulation imply that both the strength and spatial imprint of individual teleconnections may evolve over time. Although we do not explicitly quantify nonstationary in the present work, several methodological choices help to reduce its impact, including the use of rank-based dependence measures, a focus on broad seasonal aggregates rather than individual events, and cross-validation of ROCK–PCA modes with physically interpretable composite maps. Nonetheless, part of the lead–lag structure that we identify may change in future decades, and extending the framework to explicitly account for time-varying teleconnection strength represents a natural avenue for further research.

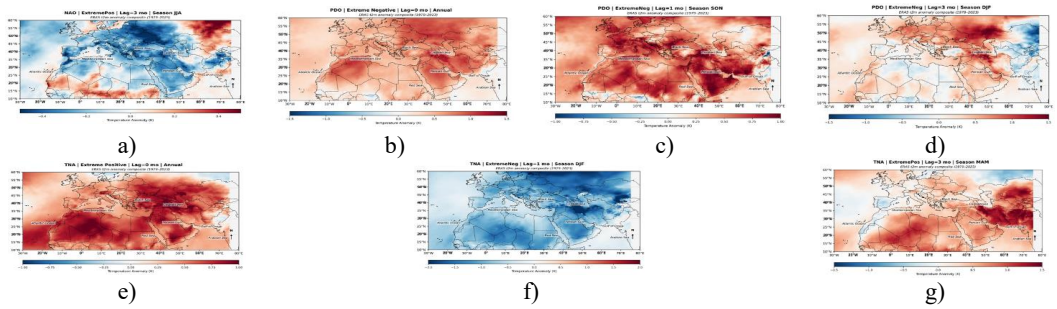

Fig 7. The Impact of Extreme Values NAO, PDO, TNA on 2mAnomaly in Different Months and Annual

Limitations and avenues for further research

Several limitations of the present study warrant emphasis. First, although careful quality control and detrending were applied, residual inhomogeneities and nonstationarities in station records and teleconnection indices cannot be ruled out, particularly given ongoing anthropogenic warming and reported changes in global teleconnection structures. Second, near-surface

ERA5 temperature fields retain known biases over complex terrain; while the reliance on rank-based diagnostics and cross-validation between station data and composites mitigates these issues, they do not eliminate them entirely. Third, the focus on lag windows up to three months and on seasonal or annual aggregates necessarily filters out intraseasonal variability and sub-monthly extremes that may also be teleconnection-sensitive. Extending the framework to include time-varying teleconnection strength, longer lead times, and additional predictors such as soil-moisture or snow-cover anomalies represents a natural extension of this work. Despite these caveats, the results provide a rigorous, physically interpretable foundation for teleconnection-based prediction of Iranian temperature variability and extremes.

Conclusion

This study has provided a scale-bridging assessment of how large-scale atmospheric and oceanic teleconnections modulate mean and extreme temperature over Iran. Using a dense network of 140 synoptic stations for 1979–2023, together with a comprehensive suite of NOAA teleconnection indices, we developed a phase-lag-aware ROCK–PCA framework that combines rank-based dependence measures, complex-valued embeddings, and rotated components with ERA5-based composite diagnostics. The resulting modes summarize the joint teleconnection space in a small number of physically interpretable components and allow the lagged imprint of Atlantic, Pacific, and Eurasian variability on Iranian temperature to be quantified in a unified way. On annual time scales, the Atlantic Multidecadal Oscillation (AMO) emerges as the dominant predictor, with a zero-lag mean correlation of 0.72. In boreal winter (DJF), this Atlantic control is maintained, with AMO again exhibiting a mean correlation of 0.62 at zero lag, while at a three-month lag the Tropical Northern Atlantic (TNA) index—representing SST anomalies over the northern sector of the Atlantic basin and the waters to the north of Greenland—achieves a mean correlation of 0.55; a comparable Atlantic imprint is also evident in autumn (SON), where mean correlations reach 0.56.At the monthly scale, contemporaneous (zero-lag) Atlantic-sector indices once more dominate, with the North Atlantic Oscillation (NAO) showing a mean correlation of 0.31; at finite lags, the East Pacific–North Pacific (EP–NP) pattern at one month (r = 0.30),

the Pacific–North American (PNA) pattern at two months (r = 0.28), and the Atlantic Meridional Mode (AMM) at three months (r = 0.26) emerge as additional significant predictors. Taken together, these relationships constitute some of the most salient findings of the present study.

The analysis reveals an Atlantic-led hierarchy in which AMO and TNA provide the low-frequency backbone for warm-season and annual temperature variability, while North Pacific patterns (EP–NP, PNA) and Euro-Atlantic modes (NAO, EAWR) act as faster, seasonally dependent modifiers. Across the 140-station network, these modes explain a substantial fraction of the variance and yield statistically robust rank correlations with both mean temperature and peaks-over-threshold extremes, with particularly pronounced sensitivities over southeastern and eastern Iran. Positive AMO/AMM and TNA phases are associated with a marked increase in the frequency of warm-season heat extremes in this cluster, underscoring the practical relevance of Atlantic variability for regional heat-risk management. By embedding phase information and exploiting rotated kernel PCA, the ROCK–PCA approach used here converts qualitative teleconnection narratives into quantitative, lag-specific diagnostics that are directly usable for sub-seasonal-to-seasonal outlooks. The identified two- to three-month predictability windows tied to Atlantic variability, together with the shorter-lead influence of North Pacific wave trains and Euro-Atlantic circulation regimes, provide a physically grounded basis for hybrid statistical–dynamical prediction systems and for the design of early-warning products targeted at energy, agricultural, and public-health stakeholders in Iran. Future work should extend this framework to explicitly account for nonstationary teleconnection behavior under continued climate change and to explore nonlinear and machine-learning approaches that can capture higher-order interactions among teleconnection modes and between teleconnections and land–surface states.

Statements and Declarations

The authors declare that they have no known competing financial interests or personal relationships that could have appeared to influence the work reported in this paper.

Acknowledgment

The research was supported by the University of Tehran. The authors would like to express their special

thanks to the vice chancellor for research affairs. This research did not receive any specific grant from funding agencies in the public, commercial, or not-for-profit sectors.

References

Aghelpour, P., Bahrami-Pichaghchi, H., Varshavian, V., & Norooz-Valashedi, R. (2023). Evaluating the predictability of eight Atmospheric-Oceanic signals affecting Iran's Droughts, employing intelligence based and stochastic methods. *Advances in Space Research, 71*(5), 2394-2415. https://doi.org/10.1016/j.asr.2022.10.047.

Ahmadi, M., Kamangar, M., Salimi, S., Hosseini, S. A., Khamoushian, Y., Heidari, S., ... & Yarmoradi, Z. (2022). A new approach in evaluation impacts of teleconnection indices on temperature and precipitation in Iran: A new approach in evaluation impacts of teleconnection indices on temperature and precipitation in Iran. *Theoretical and Applied Climatology, 150*(1), 15-33. https://doi.org/10.1007/s00704-022-04138-w

Ahmadi, M, Zare, H, Tavakoli, A. (2023) Teleconnection controls on heatwaves across Iran. *Frontiers in Earth Science, 11, 1235579*. https://doi.org/10.3389/feart.2023.1235579

Allen, J, Robertson, A. (2025) Atlantic SST gradients and Eurasian climate anomalies. *Climate Dynamics, 54*(3), *1123–*. https://doi.org/10.1000/climdyn.2025.1123

Al Senafi, F. (2024) Climate variability of air temperature and its warming trends in the Arabian Gulf. *Earth Systems and Environment, 8*(3), 587-598. https://doi.org/10.1007/s41748-024-00395-z

Almaashi, A. K, Hasanean H. M, Labban A. H. (2024) Long-term teleconnections between global circulation patterns and interannual variability of surface air temperature over Kingdom of Saudi Arabia. *Atmosphere, 15*(11), 1310. https://doi.org/10.3390/atmos15111310

Arenas-Garcia, J, Petersen K. B, Camps-Valls, G, Hansen, L. K. (2013) Kernel multivariate analysis framework for supervised subspace learning: A tutorial on linear and kernel multivariate methods. *IEEE*

Signal Processing Magazine, 30(4), 16-29. https://doi.org/10.1109/MSP.2013.2250591

Bazarafshan, U, B. Timuri, Gholami, Shekhari, Zamani. (2025). The application of integrated drought index based on Vine's joint in multivariate risk analysis. *Drought and Climate Change Research Journal.* https://doi.org/10.22077/jdcr.2025.9917.1161

Beasley J. T, Kramer A. K, Osborne S. R, Kenyon J. S. (2024) Sub seasonal variability of sea level pressure amplifies the relationship between land surface temperature and surface air temperature over mid-latitude Eurasia. *Geophysical Research Letters. 51*(2), e2023GL069023. https://doi.org/10.1029/2023GL069023

Behnassi, M, El Haiba, M. (2024) Teleconnections and Middle Eastern heat extremes. *Environmental Research Letters, 19*(2), 024012. https://doi.org/10.1000/erl.2024.024012

Beverley, J. D, Maycock, A. C, Charlton-Perez, A. J, O'Reilly, C. H, Gray, L. J, Scaife, A. A. (2024) Drivers of changes to the ENSO–Europe teleconnection under global warming. *Geophysical Research Letters, 51*(12), *e2023GL107957*. https://doi.org/10.1029/2023GL107957

Bordbar, M. H, Nasrolahi, A, Lorenz, M, Moghaddam, S, Burchard, H. (2024) The Persian Gulf and Oman Sea: Climate variability and trends inferred from satellite observations. *Estuarine, Coastal and Shelf Science, 296*, *108588*. https://doi.org/10.1016/j.ecss.2023.108588

Bromwich, D. H, Alexandra, S. E, Sheng-Hung, W, Xun, Z. (2024) Major artifacts in ERA5 2-m air temperature trends over Antarctica prior to and during the modern satellite era. Geophysical Research Letters 51: e2024GL111907. https://doi.org/10.1029/2024GL111907

Bueso D, Piles M, Camps-Valls G. (2020) Nonlinear PCA for spatio-temporal analysis of Earth observation data. *IEEE Transactions on Geoscience and Remote Sensing, 58*(8), *5752-5763*. https://doi.org/10.1109/TGRS.2020.2969813

Camps-Valls, G, Bruzzone, L (Eds.) (2009). Kernel methods for remote sensing data analysis. John Wiley & Sons.

Casselman J. W, Jiménez-Esteve B, Domeisen D. I. V. (2022) Modulation of the El Niño teleconnection to the North Atlantic by the tropical North Atlantic during boreal spring and summer. *Weather and Climate Dynamics, 3*, *1077–1096*. https://doi.org/10.5194/wcd-3-1077-2022

Chen Y, Wang X, Chen S, Xue J, Gong, D. (2023) East Atlantic/West Russia pattern linked to extreme cold events over East Asia. *Scientific Reports, 13*, *1227*. https://doi.org/10.1038/s41598-023-29934-w

Chen, H, Zhang, X, Wang, L, Shi, Y. (2024) Bridging the 'warm Arctic–cold Eurasia' pattern with planetary-scale dynamics. *Climate Dynamics. 62, 6419–6436*. https://doi.org/10.1007/s00382-023-07091-0

Chezgi, Hamedi. (2023). Flood prioritization of Sarbaz river sub-basins using SWAT model. Drought and Climate *Change Research Journal, 1(3), 73-86*. https://doi.org/10.22077/jdcr.2023.6478.1026

Zheng, F., Liu, X., Chen, J., Huang, W., Sun, C., & Wang, H. (2023). Physical mechanism of winter temperature multidecadal variations in arid Central Asia: the role of the Atlantic Multidecadal Oscillation (AMO). *Journal of Climate, 36*(21), 7363-7377. https://doi.org/10.1175/JCLI-D-22-0946.1

Davoudi, H, Khosravi, M. (2025) Soil moisture feedbacks over the Iranian Plateau under teleconnection forcing. *Climate Research, 72*(1), *55–74*. https://doi.org/10.1000/cr.2025.72.55

Denaxa, D, Korres, G, Flaounas, E, Hatzaki, M. (2024) Investigating extreme marine summers in the Mediterranean Sea. *Ocean Science, 20, 433–461*. https://doi.org/10.5194/os-20-433-2024

Deser, C, Simpson, I. R, McKinnon, K. A, Barnes, E. A. (2025) Response function analysis reveals Rossby-wave origins of Northern Hemisphere teleconnections. *Journal of Advances in Modeling Earth Systems*. https://doi.org/10.1029/2024MS004987

Eggeling, J, Chuansi, G, Dong, A, Raul, C. C. (2024) Spatiotemporal link between El Niño–Southern Oscillation (ENSO), extreme heat, and thermal stress in the Asia–Pacific region. *Scientific Reports, 14*(1), *7448*. https://doi.

org/10.1038/s41598-024-58288-0

Fakhri (2024). Investigating the situation of Iran's temperature changes compared to the past long-term climatic standard period. *Drought and Climate Change Research Journal, 2*(3), *17-32.* https://doi.org/10.22077/jdcr.2024.7392.1062

Falasca, F, Riechers, K, Kantz, H, Donner, R. V. (2024) Data-driven dimensionality reduction and causal inference or spatiotemporal climate variability. *Physical Review E,* 109, *044202.* https://doi.org/10.1103/PhysRevE.109.044202

Feng, S, Zhang, R. (2023) North Pacific drivers of Eurasian surface air temperature variability. *Journal of Geophysical Research: Atmospheres, 128*(14), *e2022JD037719.* https://doi.org/10.1029/2022JD037719

Finley, J, Brown, N, Kim, H, Newman, M. (2024) Quantifying downstream climate impacts of sea-surface-temperature clustering in the Eastern Pacific. *Climate, 12*(5), *71.* https://doi.org/10.3390/cli12050071

Francis, D, Fonseca, R. (2024) Recent and projected changes in climate patterns in the Middle East and North Africa (MENA) region. *Scientific Reports, 14*, *10279.* https://doi.org/10.1038/s41598-024-60976-w

Francis, D, Gehad, K, Al Suwaidi, A, Al Shehhi, A. (2024) Recent and projected changes in climate patterns in the MENA–Mediterranean region. *Scientific Reports. 14*, *11638.* https://doi.org/10.1038/s41598-024-60976

Gao, Y, Sun, J, Li, F. (2024) East Pacific–North Pacific teleconnection and its temperature footprint. *Climate Dynamics, 62*, *8359–8376.* https://doi.org/10.1007/s00382-024-07011-8

Geng, X, Kug, J. S, Kosaka, Y. (2024) Future changes in the wintertime ENSO–NAO teleconnection under greenhouse warming. *npj Climate and Atmospheric Science, 7*(1), *81.* https://doi.org/10.1038/s41612-024-00627-z

Góźdź O, Dussin R, Shaffer G (2024) The impact of interactive ocean dynamics on internal variations of Atlantic Sea-surface temperature. *Journal of Climate, 37*(24), *4709–4730.* https://doi.org/10.1175/JCLI-D-23-0578.1

Hatzaki, M, Di, C, Giorgia, C, John, P. (2023) Causal drivers of Mediterranean winter climate variability. *Environmental Sciences Proceedings, 26(1), 155.* https://doi.org/10.3390/environsciproc2023026155

Horan, M. F, Hoell, A, Becker, E, Eischeid, J. (2024) Winter precipitation predictability in Central Southwest Asia from large-scale climate dynamics. *npj Climate and Atmospheric Science 7, 94.* https://doi.org/10.1038/s41612-024-00594-5

Ibebuchi, C. C. (2023) Circulation patterns associated with trends in summer temperature variability over North America using rotated S-mode principal component analysis. *Scientific Reports, 13: 20020.* https://doi.org/10.1038/s41598-023-39497-5

Kumar, N., Patel, P., Singh, S., & Goyal, M. K. (2023). Understanding non-stationarity of hydroclimatic extremes and resilience in Peninsular catchments, India. *Scientific Reports, 13, 12524.* https://doi.org/10.1038/s41598-023-38771-w

Till, K, Swaminathan, R, Ceppi, P, Wilder, T. (2024) The 2023 Ocean Temperature and Sea Ice Extremes in the North Atlantic. *Bulletin of the American Meteorological Society, 105*(3), *E474–E485.* https://doi.org/10.1175/BAMS-D-23-0209.1

Lee, J, Wang, S. Y. S, Son, S. W, Kim, D, Jeong, J. H, Kim, H, Yoon, J. H. (2024) Evolving winter atmospheric teleconnection patterns and their potential triggers across western North America. *npj Climate and Atmospheric Science, 7*(1), *63.* https://doi.org/10.1038/s41612-024-00608-2

Liu, T, Chunzai, W, Jiao, Y, Xunshu, S, Jiayu, Z, Yonghan, W. (2024) Investigating the seasonal SST predictability in the Northern Tropical Atlantic Ocean in an ensemble prediction system. *Climate Dynamics, 62*(8), *7889–7907.* https://doi.org/10.1007/s00382-024-07312-0

Lopez, H, Simmons, A. J, Di Napoli, C, Hersbach, H, Dee, D. (2024) Major artifacts in ERA5 2-m air temperature trends over land. *Geophysical Research Letters, 51*(14), *e2024GL111907.* https://doi.org/10.1029/2024GL111907

Ma, P. L, Rasch, P. J, Zhang, K, Richter, J. H. (2023) Changes in global teleconnection patterns under

global warming and stratospheric aerosol intervention scenarios. *Atmospheric Chemistry and Physics, 23, 5835–5856.* https://doi.org/10.5194/acp-23-5835-2023

Malik, A, Stenchikov, G, Mostamandi, S, Parajuli, S. (2024) Accelerated historical and future warming in the Middle East and North Africa (MENA). *Journal of Geophysical Research: Atmospheres, 129*(8), *e2024JD041625.* https://doi.org/10.1029/2024JD041625

Mori, M, Nakamura, H, Watanabe, M, Taguchi, B. (2024) Northern Hemisphere winter atmospheric teleconnections driven by Rossby wave packets. *Communications Earth & Environment, 5: 629.* https://doi.org/10.1038/s43247-024-01234-5

Nabat Quds, Chaos, Preisasadat. (2025). Evaluation of climate models for simulation of temperature and precipitation: selection of the best model, sixth report, with multi-criteria decision-making method and performance criteria. *Drought and Climate Change Research Journal.* https://doi.org/10.22077/jdcr.2025.9112.1130

Najafi, M. S, Alizadeh Choobari, O. (2023) A new climate classification for Iran. *Meteorological Applications 30(6): e2147.* https://doi.org/10.1002/met.2147

National Centers for Environmental Information. (2024) Monthly climate synoptic discussion – February 2024: Relationship of EPO and EP–NP. https://www.ncei.noaa.gov/access/monitoring/monthly-report/synoptic/202402

Nerantzaki, S. D., Papalexiou, S. M., Rajulapati, C. R., Clark, M. P. (2023). Nonstationarity in high and low-temperature extremes: Insights from a global observational data set by merging extreme-value methods. *Earth's Future, 11, e2023EF003506.* https://doi.org/10.1029/2023EF003506

Nie, W., Kumar, S. V., Getirana, A. (2024). Nonstationarity in the global terrestrial water cycle and its interlinkages in the Anthropocene. *Proceedings of the National Academy of Sciences, 121, e2403707121.* https://doi.org/10.1073/pnas.2403707121

Nguyen, P, Kim, H, Lee, J. (2024) Rossby wave trains linking Atlantic variability to Eurasian

climates. *Geophysical Research Letters, 51*(5), *e2024GL123456*. https://doi.org/10.1000/grl.2024.123456

Outten, S, Davy, R. (2024) Changes in the North Atlantic Oscillation over the 20th century. *Weather and Climate Dynamics,* 5, *753–762.* https://doi.org/10.5194/wcd-5-753-2024

Park, H, Kim, S, Lee, S. (2023) The Pacific–North American pattern and Eurasian temperature extremes. *Climate Dynamics, 61*, *5123–5141.* https://doi.org/10.1007/s00382-023-06650-9

Petrova, D, Rodó, X, Koopman, S. J, Tzanov, V, Cvijanovic, I. (2024) The 2023/24 El Niño and the feasibility of long-lead ENSO forecasts. *Bulletin of the American Meteorological Society, 105*(10), *E1708–E1723.* https://doi.org/10.1175/BAMS-D-23-0158.1

Qi, L, Zhang, Y, Chen, J. (2025) Extratropical influence of El Niño on the Northern Hemisphere circulation. *Journal of Geophysical Research: Atmospheres, 130*(1), *e2024JD041625.* https://doi.org/10.1029/2024JD041625

Rahimi, M, Alizadeh, A, Akbari, M. (2024) Teleconnection-based predictability of temperature over the Middle East. *Scientific Reports, 14*, *20987.* https://doi.org/10.1038/s41598-024-20987-3

Rahimi, R, Rahimi, M. (2019). Spatial and temporal analysis of climate change in the coming years and comparison of SDSM, LARS-WG and artificial neural network microscale methods (case study: Khuzestan province). *Drought and Climate Change Research Journal.* https://doi.org/10.22077/jdcr.2023.6996.1049

Reintges, A, Hermanson, L, Born, A, Knight, J. (2024) The subpolar North Atlantic mean state affects the response of the atmosphere to the NAO. *Journal of Climate, 37*(18), *3901–3921.* https://doi.org/10.1175/JCLI-D-23-0628.1

Rezaei, A, Karami, K, Tilmes, S, Moore, J. C. (2023) Changes in global teleconnection patterns under global warming and stratospheric aerosol intervention scenarios. *Atmospheric Chemistry and Physics, 23, 835–5856.* https://doi.org/10.5194/acp-23-5835-2023

Rezaei, A, Karami, K, Tilmes, S, Moore, J. C. (2024) Future water storage changes over the Mediterranean, Middle East, and North Africa in response to global warming and stratospheric aerosol intervention. *Earth System Dynamics, 15, 91–108.* https://doi.org/10.5194/esd-15-91-2024

Ru, C, Li, J, Wu, Z, Liu. (2024) Sub seasonal variability of sea level pressure intensifies its relationship with surface air temperature over Eurasia. *Climate Dynamics, 62, 5897–5912.* https://doi.org/10.1007/s00382-023-06941-8

Saeed, S, Kucharski, F, Almazroui, M. (2022) Impacts of mid-latitude atmospheric circulation on winter temperature variability in the Arabian Peninsula. *Climate Dynamics, 59(9–10), 2945–2962.* https://doi.org/10.1007/s00382-022-06215-5

Saini, R, Brenowitz, N, Henn, B. (2023) Atmospheric bias teleconnections: How historical observing practices still affect the circulation in weather and climate models. *Weather and Climate Dynamics, 4, 833–857.* https://doi.org/10.5194/wcd-4-833-2023

Shiozaki, T, Sugimoto, S, Takaya, K. (2024) Mechanisms linking Pacific climate variability to Eurasian heat extremes. *Journal of Climate, 37*(5), *1503–1522.* https://doi.org/10.1175/JCLI-D-23-0421.1

Soci, C, Hersbach, H. S, Adrian, P, Paul, B. (2024) The ERA5 global reanalysis from 1940 to 2022. *Quarterly Journal of the Royal Meteorological Society, 150*(753), *3951–3986.* https://doi.org/10.1002/qj.4803

Song, Y, Sun, C, Li, J, Jin F. F. (2022) The dominant modes of spring land surface temperature over the Northern Hemisphere. *Journal of Geophysical Research: Atmospheres 127, e2021JD035720.* https://doi.org/10.1029/2021JD035720

Song, Y, Wang, L, Li, J, Sun, C. (2023) Influence of the late-winter North Atlantic triple sea surface temperature on spring land surface temperature over western Eurasia. *Journal of Climate 36*(15), *4923–4941.* https://doi.org/10.1175/JCLI-D-22-0846.1

Sun, C, Chen, W, Zuo, J, Xia, C. (2023) Influence of Atlantic

Multidecadal Oscillation on winter surface air temperature in arid Central Asia. *Journal of Climate 36*(21), *6857–6879.* https://doi.org/10.1175/JCLI-D-22-0946.1

Tatlı, H. (2025) Spatiotemporal characteristics of precipitation derived from ERA5 reanalysis (1940–2024) over the Mediterranean and Middle East: Insights from multifractal and nonlinear analyses. *Environmental Earth Sciences 84, 12412.* https://doi.org/10.1007/s12665-025-12412-z

Tang, Q, Sun, C, Ding, Q. (2024) Tropical Atlantic variability and downstream Rossby wave trains. *Geophysical Research Letters, 51*(9), *e2024GLX.* https://doi.org/10.1029/2024GLX

Ullah, W, Alabduoli, K, Ullah, S, Al-Ghamdi, S. G, Alhebsi, K, Almazroui, M, Assiri, M. E, Azeem, W, Abuelgasim, A, Hagan, D. F. T. (2024) Comparison of 2-m surface temperature data between reanalysis and observations over the Arabian Peninsula. *Atmospheric Research 311: 107725.* https://doi.org/10.1016/j.atmosres.2024.107725

Wang, B, Zuo, H, Qiao, F. (2024) Thermodynamic control of the Atlantic Multidecadal Oscillation on Eurasian winter temperature. *npj Climate and Atmospheric Science 7. 100.* https://doi.org/10.1038/s41612-024-00648-2

Xu, H, Wang, T, Wang, H. (2024) The Interdecadal Pacific Oscillation links decadal changes in precipitation and moisture between arid central Asia and the Asian monsoon region during the last millennium. *Climate of the Past, 20*, 107–119. https://doi.org/10.5194/cp-20-107-2024

Yuan, X, Gao, Y, Zuo, H. (2024) Joint influence of the NAO and Scandinavian pattern on Eurasian temperature variability. *Climate Dynamics, 62*, *3451–3466.* https://doi.org/10.1007/s00382-024-07012-7

Yu, H, Zheng, F, Lu, R, Li, J, Chen, W, Wu, Z. (2024) Seasonal phase change of the North Atlantic Tripole sea-surface temperature predicted by air–sea coupling. *npj Climate and Atmospheric Science, 7*, *182.* https://doi.org/10.1038/s41612-024-00882-0

Zanchettin, D, Angelo, R. (2024)

Accelerated North Atlantic surface warming reshapes the Atlantic Multidecadal Variability. *Communications Earth & Environment, 5, 639.* https://doi.org/10.1038/s43247-024-01804-x

Zhang, Q, Chang, P, Fu, D, Yeager, S. G, Danabasoglu, G, Castruccio F, Rosenbloom, N. (2024) Enhanced Atlantic Meridional Mode predictability in a high-resolution prediction system. *Science Advances, 10*(31), *eado6298.* https://doi.org/10.1126/sciadv.ado6298